Chemical Science

ROYAL SOCIETY OF CHEMISTRY

EDGE ARTICLE

View Article Online
View Journal | View Issue

Cite this: *Chem. Sci.*, 2023, **14**, 13924

All publication charges for this article have been paid for by the Royal Society of Chemistry

Received 14th October 2023
Accepted 17th November 2023

DOI: 10.1039/d3sc05461f

rsc.li/chemical-science

Manipulating the crystal plane angle within the primary particle arrangement for the radial ordered structure in a Ni-rich cathode†

Ting Chen,[a] Chuyao Wen,[b] Chen Wu,[c] Lang Qiu,[d] Zhenguo Wu, *[d] Jiayang Li,[b] Yanfang Zhu,[b] Haoyu Li,[d] Qingquan Kong,[a] Yang Song,[d] Fang Wan,[d] Mingzhe Chen,[e] Ismael Saadoune,[f] Benhe Zhong,[d] Shixue Dou,[g] Yao Xiao *[b] and Xiaodong Guo*[ad]

Ni-rich cathodes with a radial ordered microstructure have been proved to enhance materials' structural stability. However, the construction process of radial structures has not yet been clearly elaborated. Herein, the formation process of radial structures induced by different doped elements has been systematically investigated. The advanced Electron Back Scatter Diffraction (EBSD) characterization reveals that W-doped materials are more likely to form a low-angle arrangement between crystal planes of the primary particles and exhibit twin growth during sintering than a B-doped cathode. The corresponding High Angle Annular Dark Field-Scanning Transmission Electron Microscopy (HAADF-STEM) analysis further proves that the twin growth induced by W doping can promote the migration of Li^+. Simultaneously, the W-doped sample reduces the (003) plane surface energy and promotes the retention of the crystal plane, which can effectively alleviate the structural degradation caused by Li^+ (de) intercalation. At a cut-off voltage of 4.6 V, the W-doped cathode displays a capacity retention rate of 94.1% after 200 cycles at 1C. This work unveils the influence of different element doping on the structure from the perspective of crystal plane orientation within primary particles and points out the importance of the exposure and orientation of the crystal plane of the particles.

1 Introduction

The energy density, power density, and cycle and safety performance of cathodes have become the bottleneck of current lithium-ion batteries (LIBs).[1,2] With the demand for low-cobalt/cobalt-free cathodes and the commercialization of NCM811, increasing Ni content and enhancing cut-off voltage are effective ways to improve the energy density of NCM cathode materials.[3,4] Compared to low nickel cathodes, Ni-rich cathodes face more serious challenges such as intragranular/intergranular cracks, structural degradation and interface side reactions.[5–7] Simultaneously, the high cut-off voltage condition will further aggravate particle cracking, interface side reactions and structural degradation,[8,9] and ultimately induce rapid electrochemical performance degradation.[10,11] Unfortunately, a higher cutoff voltage results in stronger anisotropic strain inside the material, especially in the *c*-axis direction, leading to more severe particle fracture.

Some works show that Ni-rich cathodes with the radially ordered arrangement structure of primary particles can effectively alleviate stress accumulation.[12–14] The special structure can significantly relieve local stress concentration, and make a single primary particle uniformly shrink and expand during the cycle, thus minimizing local stress accumulation and inhibiting microcracks.[15] Interestingly, this unique structure can be regulated by element doping. For example, a B-doped Ni-rich cathode can reduce the surface energy of the (003) plane, showing primary particle refinement and radially ordered arrangement.[16–18] Additionally, Sn, Ta, Nb, W, Mo *etc.* doped Ni-based cathodes can also obviously control the primary particle growth, displaying a radially ordered structure.[19–21] Furthermore, Ni-rich cathodes with concentration gradient structures

[a]*Institute for Advanced Study, Chengdu University, Chengdu, 610106, PR China. E-mail: xiaodong2009@scu.edu.cn*

[b]*Institute for Carbon Neutralization, College of Chemistry and Materials Engineering, Wenzhou University, Wenzhou, 325035, PR China. E-mail: xiaoyao@wzu.edu.cn*

[c]*Research Institute of Natural Gas Technology, PetroChina Southwest Oil & Gasfield Company, Chengdu, 610299, PR China*

[d]*College of Chemical Engineering, Sichuan University, Chengdu, 610065, PR China. E-mail: zhenguowu@scu.edu.cn*

[e]*School of Energy and Power Engineering, Nanjing University of Science and Technology, Nanjing, 210094, PR China*

[f]*Applied Chemistry and Engineering Research Centre of Excellence (ACER CoE), Mohammed VI Polytechnic University, Benguerir, 43150, PR Morocco*

[g]*Institute of Energy Materials Science, University of Shanghai for Science and Technology, Shanghai, 200093, PR China*

† Electronic supplementary information (ESI) available. See DOI: https://doi.org/10.1039/d3sc05461f

can also achieve radial ordered arrangement of primary particles, but the preparation process is complex.[22–24] Therefore, based on the material preparation process, the special structure regulated by doping is more convenient. However, there is still a lack of systematic research on the effects of the geometric structure and angle driven arrangement differences of primary particles, as well as the preferred orientation of crystal planes, on the radial ordered structure of Ni-rich cathodes. And this is of great significance for stabilizing the structure of Ni-rich cathodes.

In this work, B-doped and W-doped Ni-rich cathodes ($LiNi_{0.86}Co_{0.08}Mn_{0.06}O_2$) were used to analyze the formation process in a radial ordered structure. The differences in the geometric structure, crystal plane distribution, and crystal orientation angle of primary particles in radial structures doped with different elements, as well as the influence of the differences in primary particle arrangement in radial ordered structures on the electrochemical performance of nickel rich cathodes, were analyzed. Compared with the B-doped Ni-rich cathode, the W-doped Ni-rich cathode not only has the common characteristics of (0001) crystal plane aggregation, but also has the advantages of more elongated needle-like particles and crystal twin growth with lower crystal plane orientation angle, and ultimately improves its cycle retention rate, maintaining it at 94.1%.

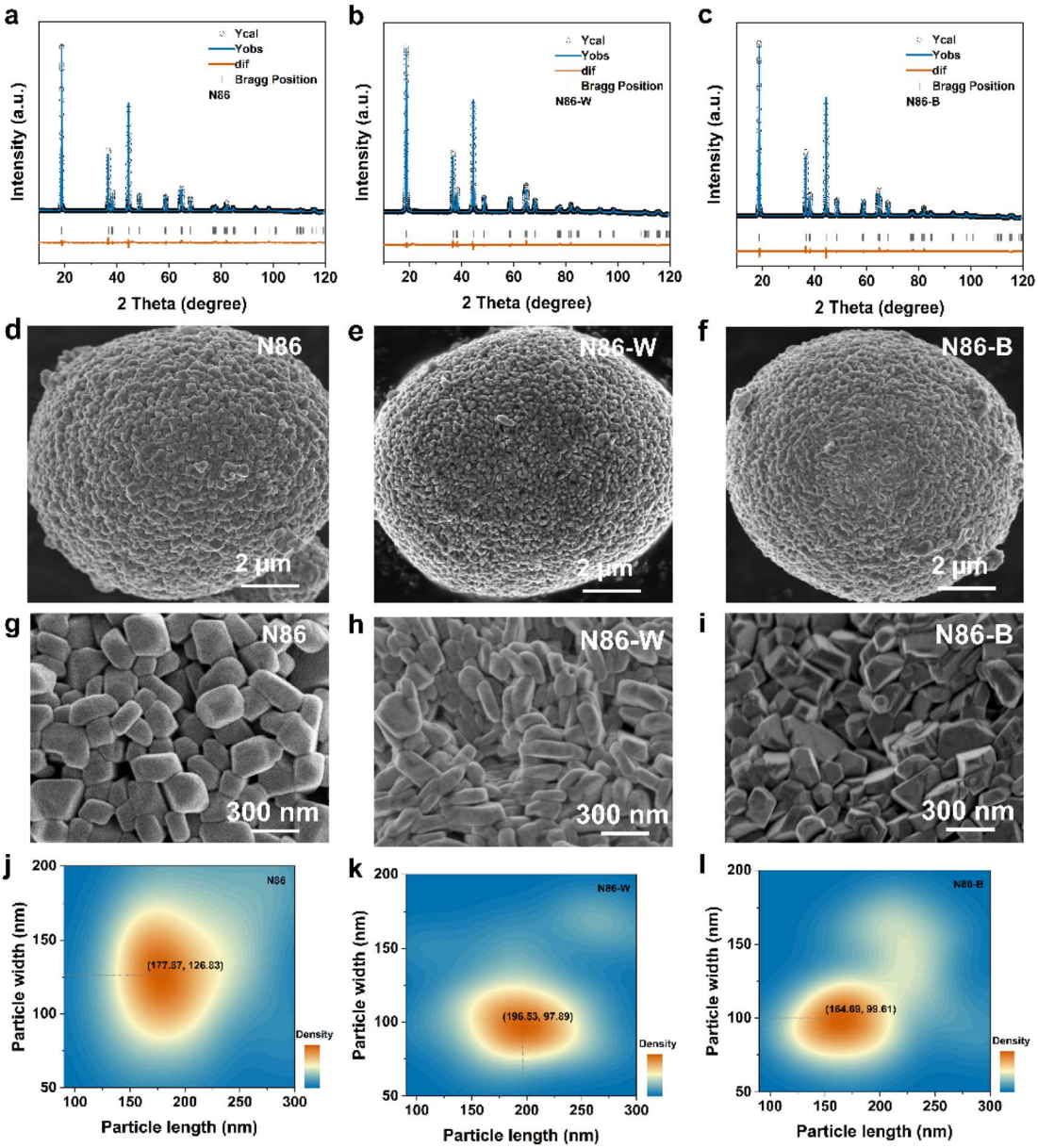

Fig. 1 (a–c) XRD powder diffraction refinement patterns for N86, N86-W, and N86-B. (d–f) SEM images of secondary particles and (g–i) primary particles on the surface of the Ni-rich cathode modified by different ion doping. (j–l) Statistics of the aspect ratio of surface primary particles of N86, N86-W, and N86-B.

2 Results and discussion

2.1 Doping drives morphology evolution

The precursor ($Ni_{0.86}Co_{0.08}Mn_{0.06}(OH)_2$, NCM86) is doped with WO_3 and B_2O_3 in turn, and NCM materials are prepared under the same sintering procedure. Furthermore, all samples' crystal structures were characterized by X-ray diffraction, which shows that there is no heterogeneous phase. The sharp Bragg peaks indicate the good crystallinity of both samples as shown in Fig. 1a–c (their lattice parameters are exhibited in Table S1†). All of the materials' c/a values are greater than 4.94, and the $I_{(003)}/I_{(104)}$ values are greater than 1.2, indicating that the modified cathodes possess well layered structure with a low Li/Ni cation mixing. As shown in Fig. 1d–f, all samples are spherical secondary particles that aggregate primary particles, with a size of approximately 10 μm. Fig. 1g–i show that the W-doped material's primary particles have the smallest average size, while particles tend to be elongated, and the morphology of the doped particles is obviously different from that of the undoped particles (N86). The results indicate that the size and morphology of the secondary particles doped with elements (B and W) are similar, but the primary particles exhibit an anisotropic growth trend. Simultaneously, the statistical analysis (Fig. 1j–l) of particle length and width further proves that the introduction of element W will refine particle size. The difference in the aspect ratio of the primary particles on the surface

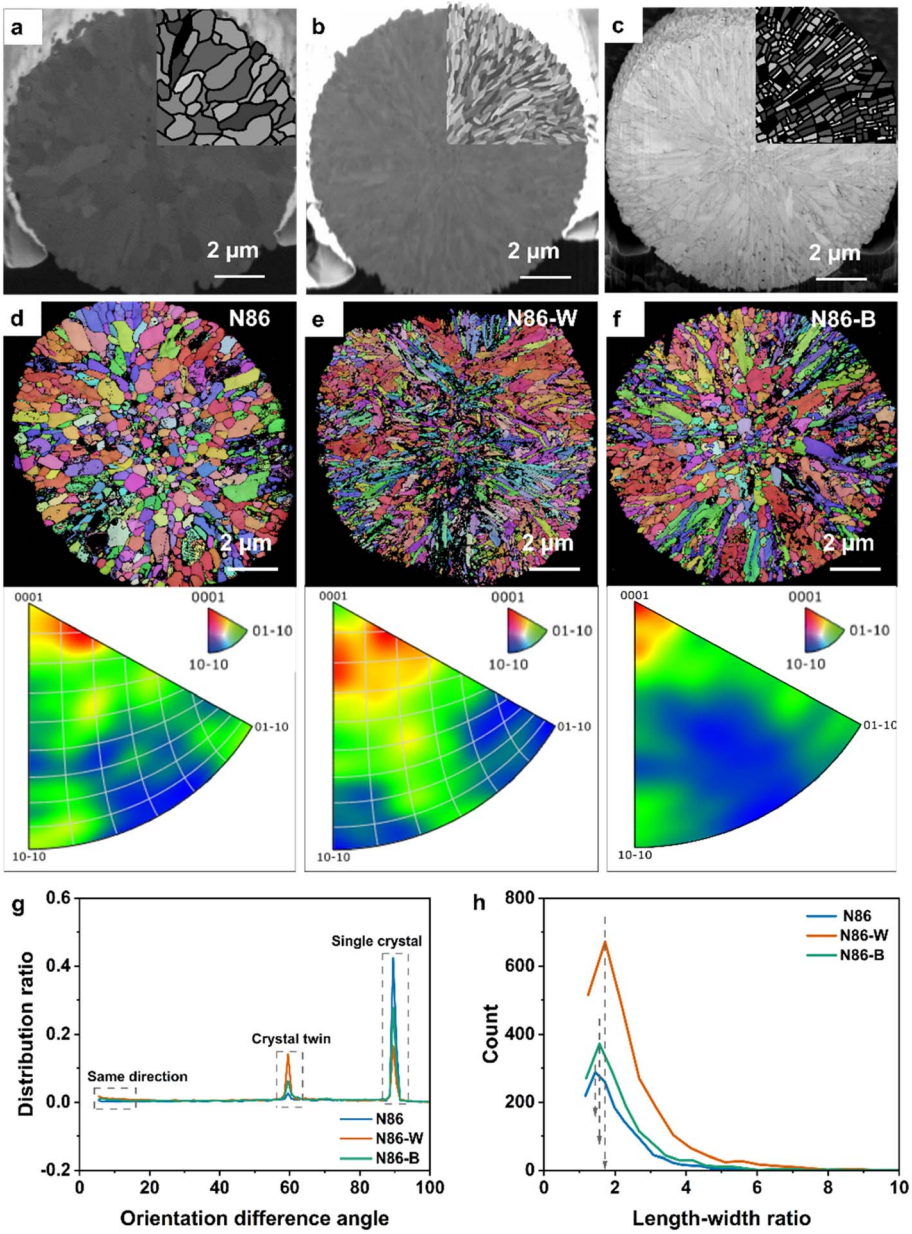

Fig. 2 (a–c) SEM images of cross sections of N86, N86-W, and N86-B. (d–f) EBSD images and crystal plane distribution of N86, N86-W, and N86-B. (g) Statistical diagram of grain length to width ratio and (h) statistical diagram of the crystal plane orientation difference angle of corresponding materials.

indicates that the W-doped particles tend to cause elongated particle aggregation with an aspect ratio of ~2, while the B-doped particles have a smaller aspect ratio of ~1.6.

2.2 Particles' macroscopic arrangement and crystal plane orientation difference

Based on the morphological differences of primary particles doped with B and W, the influence of element doping on the radial ordered structure was further analyzed. As shown in the SEM-EBSD results in Fig. 2, red, blue, and green represent (0001), (10-10), and (01-10) crystal faces, respectively. With the increase of chromatic aberration, the crystal plane angle becomes larger. The primary particles of N86 exhibit irregular shapes, and the crystal planes' orientation between adjacent grains is quite different. In contrast, the primary particles of N86-W exhibit a fine needle-like radial distribution. And the crystal plane orientations of adjacent primary particles from the outside to the inside are similar. Interestingly, the orientation angle of adjacent primary particles in N86-B from the inside to outside is between those of N86 and N86-W. By comparing the crystal plane distribution statistics of three Ni-rich cathode materials, it can be seen that the distribution of N86 internal particles in the (0001) crystal plane is relatively high, but there is also a certain distribution in the (10-10) and (01-10) crystal planes, which further indicates that there is no obvious rule for the distribution of grains in N86. The grains of N86-W are more concentrated near the (0001) crystal surface and exhibit a significant radial distribution pattern. As is well known, the highly anisotropic mechanical strain of the Ni-rich cathode during the charging and discharging process changes sharply in the *c*-axis (that is, perpendicular to the (0001) plane), so the concentrated distribution of the (0001) crystal plane promotes a more uniform stress distribution of particles during electrochemical cycling.[25] Similar crystal planes also effectively disperse the local stress of primary particles, thereby reducing the risk of stress accumulation and intergranular cracks.[26] As shown in Fig. 2g, the orientation difference angle of N86 is concentrated at 90°, indicating that the primary crystal particles are mainly distributed in the form of single crystals, with each single crystal perpendicular to the others. The mutually perpendicular crystal planes not only increase the Li^+ diffusion path, but also increase the grain boundary energy barrier in the process of ion diffusion. In addition, the high angle arrangement of crystals makes it easy for stress to accumulate during crystal shrinkage, ultimately leading to grain boundary cracking. The orientation difference of N86-W is 60° and 90°, corresponding to the twins and single crystal respectively, which indicates that W-doping causes the primary particles to exhibit twin growth. Because the twin boundary is a special low energy interface, it can effectively reduce the diffusion barrier of Li^+ on the crystal plane, thereby accelerating the diffusion of Li^+ and alleviating the stress accumulation at the grain boundary.[27,28]

Therefore, according to thermodynamic theory, the introduction of W leads to a trend of low configuration energy during material growth, while the heating of the material reduces the system energy, which may be one of the reasons why primary particles do not grow. The specific surface area and face-to-face contact area of twin nanocrystals are smaller than those of single crystals, which indicates that it is easier to agglomerate during recycling, thus showing better electrochemical stability. Through the aspect ratio analysis (Fig. 2h), the statistical size peak of the length to width ratio of N86 is about 1.4, and the ratio of N86-W is more than 1.7, while the peak of the length to width ratio of N86-B is between those of the N86 and N86-W. The above results show that N86-W particles are radial needle-like shaped. In addition, the radial needle shape of the fine particles can also achieve the purpose of deflecting crack growth and releasing strain energy through the boundary network between particles, thereby inhibiting crystal cracking. The above results further reveal the reason why the radial fine needle morphology is formed by W-doping.

2.3 Radial morphology growth mechanism

To further explore the causes of the formation of radial morphology, N86 cathode materials under different sintering atmospheres (including air and oxygen atmospheres) were analyzed. The morphology of the precursor is shown in Fig. S1.† The materials synthesized in both oxygen and air atmospheres exhibit standard α-$NaFeO_2$ with hexagonal layered structure and no obvious impurity phases (Fig. S2†), but the layered structure of the material forms faster in an oxygen atmosphere. It is obvious that the primary particles prepared by sintering in an air atmosphere are stacked in a regular sheet shape (Fig. S3†). This result indicates that the radial growth of primary particles can be achieved by controlling the crystal growth rate and inheriting the precursor morphology at the same sintering temperature. Moreover, cathodes were thermogravimetrically tested to explore the reason for the formation of a fine needle-like radial structure. As shown in Fig. S4,† it is obvious that B-doping has little effect on the decomposition of the precursor. However, the decomposition temperature of N86-W shifted slightly to the high temperature range, indicating that W-doping inhibited the decomposition rate of precursor.

By comparing the quenching results of the samples (N86, N86-W, and N86-B) at the sintering temperature range (Fig. 3), we observed the formation process of the fine needle-like radial structure at the high temperature range. When the samples were pre-calcined at 480 °C for 5 h, they were continued to be heated up to 600, 700, 750, 850 and 950 °C for quenching. The primary particles of the doped N86-W and N86-B are different from those of undoped N86, and their primary particles appear thinner and longer at 600 °C. Within 750 °C, all inherited the morphology of the precursor itself, showing a short sheet growth state. However, the introduction of doped elements will make the particles slenderer, and the length to width ratio of N86-W is the largest. As the temperature continues to rise, the primary particles of N86 and N86-B exhibit equiaxed growth, gradually changing from flaky to polyhedral, until the band/needle shape completely disappears. However, the primary particles of N86-W did not grow rapidly. After further heating to 950 °C, the size of the primary particles of N86-B and N86 was further grown, and anisotropic growth appeared in the shapes. Interestingly, the primary particles of N86-W still grow in sheet/

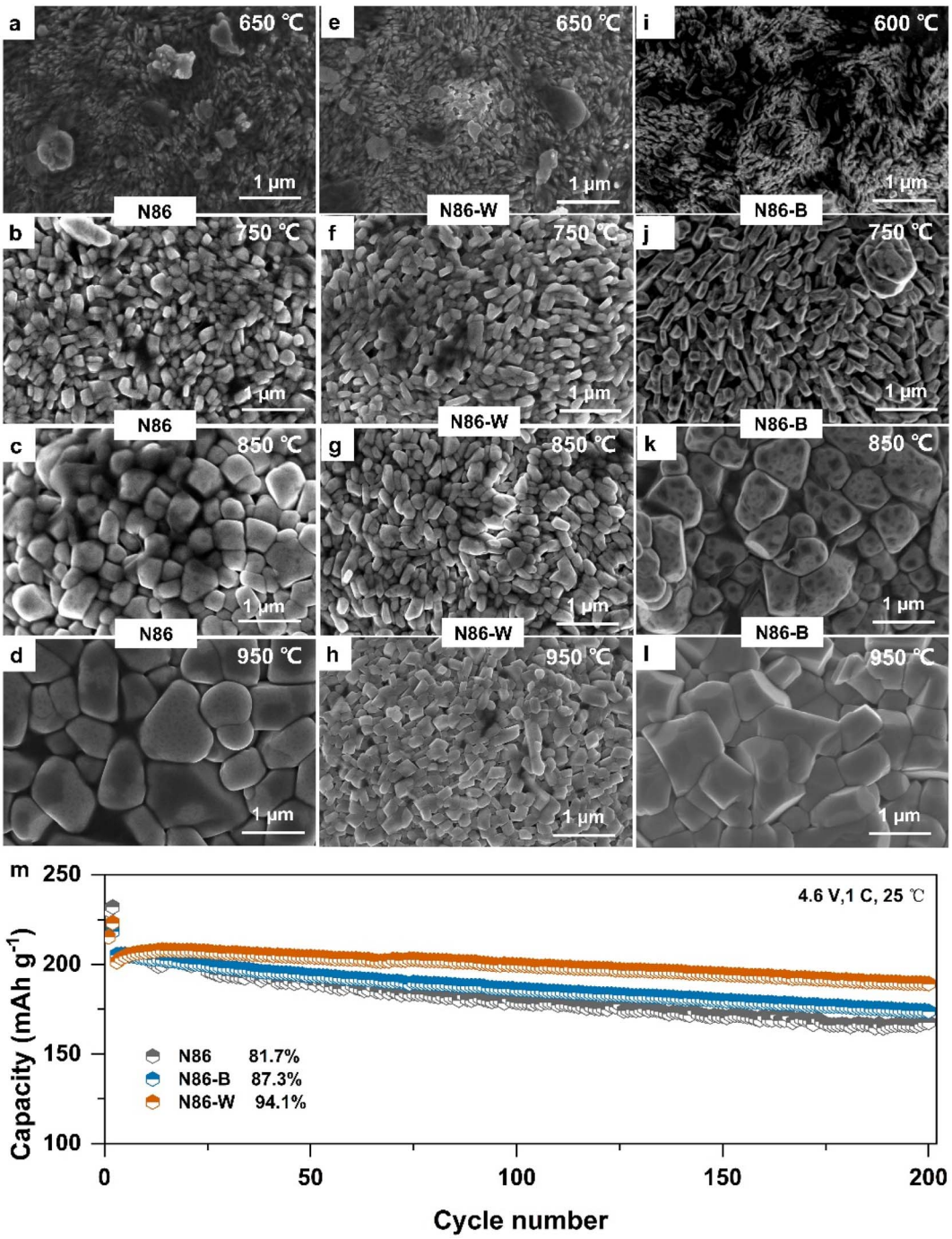

Fig. 3 SEM images of surface morphology evolution of (a–d) N86, (e–h) N86-W, and (i–l) N86-W quenched at 600, 700, 750, 800, 850, and 950 °C respectively. (m) Cyclic performance of different materials at 1C under a 3.0–4.6 V voltage window.

strip shape and becomes regular. The surface and cross section particle morphology of three kinds of samples quenched at 750 °C were further analyzed (Fig. S5†); the size of the primary particles of N86 is obviously larger than that of the other two doped samples. The primary particles of N86 are short strips, while the primary particles of N86-W and N86-B are regular strips, and N86-B is thinner. This can be seen from the internal morphology at 750 °C, showing a fine needle like growth state with introduction of elements W and B, and the particles are arranged radially from the inside out. In general, the introduction of B makes the Ni-rich cathode grow irregularly after the temperature exceeds 750 °C, and the radial morphology can only be maintained within 750 °C, while the N86-W still maintains a fine needle like radial structure at higher temperatures. Therefore, it is further confirmed that one of the reasons for the formation of fine needle-like radial structures is that W-doping inhibits the growth of primary particles. The above Ni-rich cathode materials were subjected to an electrochemical cycling test under high cut-off voltage of 4.6 V. After 200 cycles, the cycle retention of N86 is 81.7%, and

that of B and W doping is 87.31% and 94.1% respectively (Fig. 3m), and W exhibits the best cycling stability at 1C. The difference of electrochemical performance depends on the difference of Li^+ migration ability caused by the internal composition of different radial ordered structures. Simultaneously, the cycle performance of the W-doped cathode with smaller primary particles is the best. The above results explain that the influence of radial structures formed by different ion doping on the electrochemical performance is different, and the study of the evolution process of radial structures guided by ion doping becomes a key part.

The influence of temperature (480, 600, 650, 750 °C) on crystal structure can be characterized by XRD after 5 h of pre-sintering to explore the fine needle radial structure evolution during the heating process. The XRD spectrum from 480 °C to 750 °C is shown in Fig. 4a–c, and demonstrates that there is no difference in the phase transition path between the samples before and after W-doping during the heating process, and this result is also applicable to N86-B. However, the changes of $I_{(003)}/I_{(104)}$ with temperature (Fig. 4d) shows the structure evolution rates of N86-W and N86-B are obviously different. At 750 °C, $I_{(003)}/I_{(104)}$ of N86 is 1.0758, while those of N86-W and N86-B are only 0.6896 and 0.6517 respectively. In addition, the peak splitting of (006)/(012), (018)/(110) and (012)/(116) of N86-W at 750 °C is still not obvious, but the peak splitting starts to appear for N86 at 750 °C, indicating that the layered structure still exists completely for N86-W. Comparing the growth rate of the $I_{(003)}/I_{(104)}$ value of N86-W, it can be found that the growth of the (003) plane in N86-W is more inhibited than that of the (104) plane, and the results also appear in N86-B, indicating that the introduction of W and B will lead to preferential growth of the crystal plane. The above results further prove that the special radial ordered structure of W-doping is attributed to the growth rate of primary particles and the optimal growth of crystal planes. To verify the above conjecture, we calculated the surface energy of B and W-doped Ni-rich cathodes. In the $LiNiO_2$ crystal structure, the (003) planes have the lowest surface energies.[29] The surface energy of these two crystal planes mainly determines the morphology of the crystal in equilibrium state. For example, when the (003) surface dominates, the crystal presents a flat shape, while when the (104) surface dominates, it tends to present an equiaxed cubic growth shape.[30,31] In this system, all the density functional theory calculations were performed by using the Vienna *ab initio* Simulation Package (VASP) to calculate the energies of the (003) and (104) surfaces, where $LiNiO_2$ was used as a model structure to simplify the calculations (Fig. 4e). According to existing research,[32–34] a W atom enters the transition metal layer to replace a Ni atom, while B is located at the tetrahedral sites of the transition metal layer, which exists in the crystal in the form of BO^{3-}. For example, it can be obviously

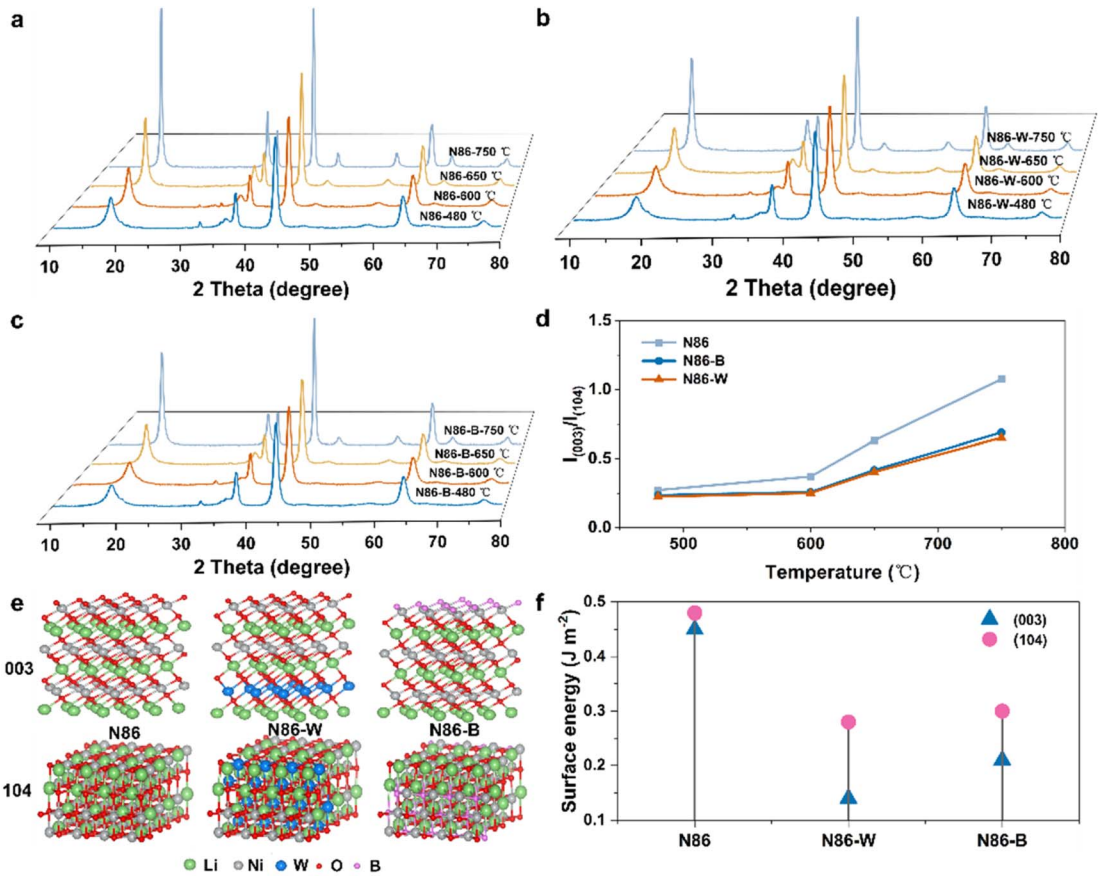

Fig. 4 (a–c) XRD patterns and (d) corresponding $I_{(003)}/I_{(104)}$ ratio of N86, N86-W and N86-B during the temperature rise from 480 to 750 °C. (e) Structural model and (f) surface energy of different crystal planes.

seen that the surface energy of the (003) facet for N86-W is much lower than that of (104) facets (Fig. 4f), indicating that the (003) face is more stable than the (104) face. Therefore, the growth rate of the (003) facet is significantly more inhibited than that of N86 and N86-B, which is consistent with the above XRD results. Meanwhile, the surface energy of the (003) crystal plane is the smallest, indicating that W doping tends to expose the (003) crystal plane in stable crystals, which is also demonstrated in Fig. S6.† The exposure of the (003) surface also laid the foundation for the fine needle formation of N86-W in the radial structure.

For the purposes of the relationship between the W doped fine needle radial structure and temperature, the morphology at different sintering temperatures was characterized by SEM. Fig. S7a–d† show the undoped Ni-rich cathode of N86 prepared by calcining at 740, 760, 800 and 850 °C for 20 h. With the increase of calcination temperature, the primary particles of N86 finished products grow, and the aspect ratio of the primary particles of all samples shows an anisotropic growth trend, and the primary particles are polygonal in shape. Fig. S7e–h† show the relationship between the morphology of N86-W and the temperature. The results demonstrate that although the primary particles in the finished product grow slightly with the increase of sintering temperature, there is a significant decrease in overall growth rate. Primary particles maintained the morphology of the precursor, and still grow in sheet form at 850 °C, but the length to width ratio of single particles decreases concurrently. The above results further indicate that the W-doped fine needle-like radial structure has obvious advantages in inhibiting the crystal growth rate of primary particles and regulating the preferential growth of crystal planes. To study whether the inhibition of this trace W-doping on crystal growth will affect the optimal sintering temperature for preparing a Ni-rich cathode, the XRD results of the annealed N86 and N86-W finished materials are shown in Fig. S8† after 20 hours of high-temperature calcination at 740, 750, 760, 770, 780 and 800 °C respectively. Therefore, W doping may have a slight impact on the rate of crystal growth, but it has an obvious impact on the optimal crystallization temperature.

The materials prepared in the range of 750–780 °C (close to the optimal sintering temperature) were tested cyclically in the 3.0–4.6 V voltage window (Fig. S9†). The initial coulombic efficiency (ICE) of N86 at different temperatures has little overall difference. However, too high sintering temperature (780 °C) will cause obvious an voltage jump in N86, which increases the barrier of Li^+ diffusion. The ICE of W doped samples at different temperatures is relatively low, because the enrichment of W element on the surface inhibits the diffusion of Li^+ at the initial reaction stage, which increases the activation period of the Ni-rich cathode.[35] In addition, the capacity of N86-W under high voltage is obviously affected by temperature. With the increase of temperature, the capacity contribution under high voltage increases significantly. In addition, the influence of temperature on the capacity of undoped N86 samples is relatively small, but the cycling performance has a certain impact. The cycling performance of the W doped Ni-rich cathode was improved at various temperatures, which further verified the outstanding advantages of fine needle like radial texture morphology in cycling. However, W doping results in high sensitivity to temperature sintering. Therefore, it is necessary to adjust the reaction temperature appropriately to construct a radial ordered structure of Ni-rich cathodes through ion doping. It is further confirmed that the fine needle like radial structure of the W doped Ni-rich cathode is the result of the combination of crystal face preference and particle growth inhibition. The geometric structure and arrangement of this special primary particle in the radial structure stabilize the nickel rich cathode. The stable electrode structure exhibits good structural stability during the charging and discharging process of the battery, and the EIS results of thermal shelving experiments are used to prove this conclusion. Fig. S10† shows that even in a deep charge state (4.6 V), the W doped Ni-rich cathode possesses a smaller charge transfer impedance (R_{ct}). Even when the battery is kept at 60 °C for 5 days after 20 cycles, its R_{ct} increase is minimal.

We further undertook a deeper exploration of the structure of N86-W at the optimum sintering temperature and carried out the high-resolution-STEM analysis of the profile, and the results are shown in Fig. 5. As shown in Fig. S11,† the uniform distribution of W element in secondary particles indicates that W enters the bulk region of the Ni-rich cathode. In the high-angle dark field of Fig. 5a, N86-W with a radial structure was clearly observed along with the particle arrangement and geometry inside the secondary particles. At higher magnification, it is found that there is an obvious grain boundary between particles. Particle regions exhibit an $R\bar{3}m$ layered structure (Fig. 5c), which is consistent with the above XRD results. Detailed high-resolution imaging of the primary particles at and near the grain boundary was carried out to detect the structural changes caused by the presence of W in detail. The enlarged HAADF images of the corresponding regions in Fig. 5b at the grain boundary are shown in Fig. 5d, where all atoms exhibit either strong bright or weak bright contrast. Combined with the STEM image simulation, we can unambiguously assign the strong contrasts to the transition metal layer and the weak bright contrasts to Ni or W atom columns. Thus, the grains at the boundary are still in an orderly layered structure, and there is obvious cation mixed arrangement. The arrangement between grains presents twin growth, and the orientation angle is less than 90°, which is conducive to the migration of Li^+.[27,36] Comparing the atomic intensity curves of line 1 and line 2 in Fig. 5e, which all show that the intensities of transition metal atoms located at the twin boundaries are weaker than those in the bulk region, the same conclusion also exists in line 3 and line 4. According to the law of grain boundary atomic column strength change, the existence of W can be expected in the twin boundaries. It can be inferred from the above results that the introduction of W makes the grains grow as twins, and the grain arrangement with smaller orientation angle weakens the migration barrier of Li^+.[37–40] At the same time, although this study indicates that W mainly enters the bulk phase within the particles, there is also a very small amount of W at the grain boundaries. Importantly, it has been reported that a small amount of W is enriched on the surface of particles in the form of oxides, which inhibits the growth of grains.[41]

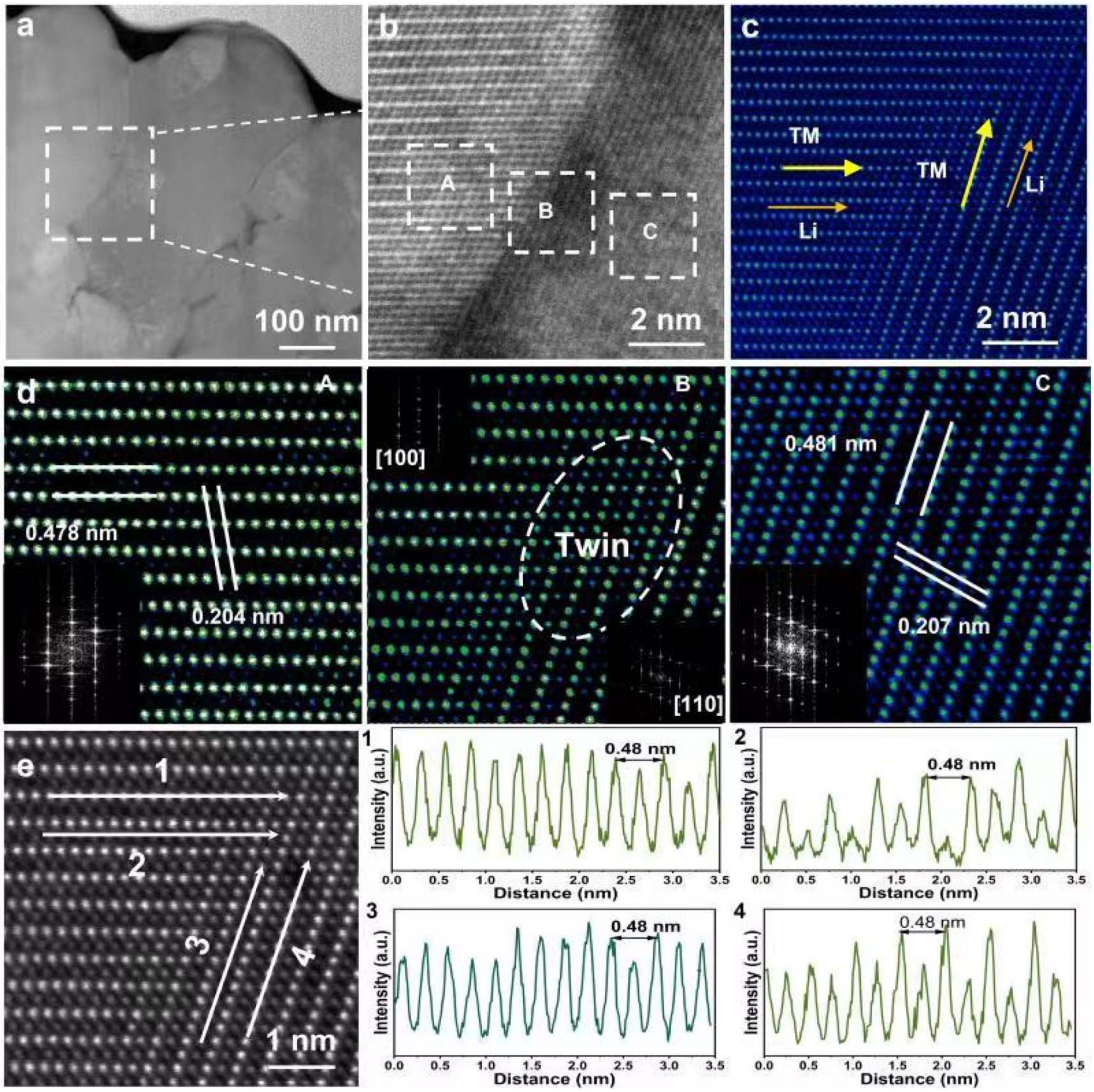

Fig. 5 (a) The HAADF image of N86-W from the middle part of the secondary particle. (b–d) The cross-sectional HAADF images of (a) and the inset represents FFT calculations of the corresponding selected area. (e) The line profiles from each selected atomic line in the HAADF image of N86-W.

3 Conclusion

In summary, this work mainly focuses on the problem that the radial morphology can effectively alleviate the particle breakage caused by the charging and discharging of a Ni-rich cathode under high voltage. The characteristics and role of the radial morphology are determined through the influence of various ion doping on the morphology and electrochemical performance. The systematic differences between the geometric structure and the arrangement of particles in the radial morphology are further explored. Comparing the radial morphology evolution mechanism of B and W doping from the perspective of thermodynamics and dynamics, W doping confirmed that high valence transition metal doping can inhibit the growth of Ni-rich particles and preferential growth of the crystal surface to achieve excellent radial morphology. The mechanism of forming a radial structure by doping different elements is different, which further affects the difference of electrochemical performance. The introduction of W can make the Ni-rich cathode have a twinning growth mode with a larger aspect ratio, smaller orientation angle and smaller primary particles, thus obtaining an excellent radial structure. This also provides ideas for the realization of an excellent radial structure by element doping in Ni-rich cathodes.

Data availability

The data underlying this study are available in the ESI.†

Author contributions

TC, CW, CW, LQ, and ZW performed the material synthesis and electrochemical tests. TC, JL, and YZ performed the DFT calculations. TC, HL, and QK performed TEM characterization. TC, YS, FW, and MC performed EBSD analysis. IS, BZ, and SD supervised the work. YX performed theoretical discussions. TC

and XG wrote the manuscript. All the authors participated in the discussions and preparation of the manuscript.

Conflicts of interest

There are no conflicts to declare.

Acknowledgements

This work was supported by the project from the National Natural Science Foundation of China [20A20145, 21878195, 21805198, 22108183], 2020 Strategic cooperation project between Sichuan University and Zigong Municipal People's Government [No. 2020CDZG-09], State Key Laboratory of Polymer Materials Engineering [No. 2020-3-02], Sichuan Provincial Department of Science and Technology [No. 2020YFG0471, No. 2020YFG0022], Sichuan Province Science and Technology Achievement Transfer and Transformation Project [No. 21ZHSF0111], Sichuan University postdoctoral interdisciplinary Innovation Fund [2021SCU12084], the start-up funding of Chemistry and Chemical Engineering Guangdong Laboratory [No. 2122010], the Transformation of Major Scientific and Technological Achievements of Central Universities in Sichuan [2022ZHCG0121], National Natural Science Foundation of China (Grant No. 52202284), Zhejiang Natural Science Foundation (Grant No. LQ23E020002), Wenzhou Natural Science Foundation (Grant No. G20220019), Cooperation between industry and education project of Ministry of Education (Grant No. 220601318235513), and the State Key Laboratory of Electrical Insulation and Power Equipment, Xi'an Jiao Tong University (EIPE22208).

References

1 P. K. Nayak, E. M. Erickson, F. Schipper, T. R. Penki, N. Munichandraiah, P. Adelhelm, H. Sclar, F. Amalraj, B. Markovsky and D. Aurbach, Review on challenges and recent advances in the electrochemical performance of high capacity Li- and Mn-Rich cathode materials for Li-ion batteries, *Adv. Energy Mater.*, 2017, **8**, 1702397.

2 W. H. Li, Y. M. Li, X. F. Liu, Z. Y. Gu, H. J. Liang, X. X. Zhao, J. Z. Guo and X. L. Wu, All-climate and ultrastable dual-ion batteries with long life achieved *via* synergistic enhancement of cathode and anode interfaces, *Adv. Funct. Mater.*, 2022, **32**, 2201038.

3 L. Y. Kong, H. X. Liu, Y. F. Zhu, J. Y. Li, Y. Su, H. W. Li, H. Y. Hu, Y. F. Liu, M. J. Yang, Z. C. Jian, X. B. Jia, S. L. Chou and Y. Xiao, Layered oxide cathodes for sodium-ion batteries: microstructure design, local chemistry and structural unit, *Sci. China: Chem.*, 2023, DOI: **10.1007/s11426-022-1550-2**.

4 T. Jin, P. F. Wang, Q. C. Wang, K. J. Zhu, T. Deng, J. X. Zhang, W. Zhang, X. Q. Yang, L. F. Jiao and C. S. Wang, Realizing Complete Solid-Solution Reaction in High Sodium Content P2-Type Cathode for High-Performance Sodium-Ion Batteries, *Angew. Chem., Int. Ed.*, 2020, **59**, 14511–14516.

5 P. Liu, T. T. Zhan, X. C. Chen, H. X. Li, Q. L. Wang, W. B. Lu and L. F. Jiao, Regulating Phase Stability of O3-Type-Layered Oxide Cathode *via* Zn^{2+} Substitution, *J. Phys. Chem. C*, 2023, **127**, 20632–20639.

6 X. Z. Zhang, G. P. Liu, K. Zhou, T. P. Jiao, Y. Zou, Q. L. Wu, X. X. Chen, Y. Yang and J. M. Zheng, Enhancing Cycle Life of Nickel-Rich $LiNi_{0.9}Co_{0.05}Mn_{0.05}O_2$ *via* a Highly Fluorinated Electrolyte Additive-Pentafluoropyridine, *Energy Mater.*, 2021, **1**, 10005.

7 L. Qiu, M. K. Zhang, Y. Song, Z. G. Wu, Y. F. Zhu, J. Zhang, D. Wang, H. Y. Hu, H. W. Li, H. R. Liu, X. B. Jia, J. Peng, S. Q. Chen, Z. G. Yang, Y. Xiao and X. D. Guo, Deciphering the degradation discrepancy in Ni-rich cathodes with a diverse proportion of [003] crystallographic textures, *Carbon Energy*, 2023, **5**, e298.

8 H. Y. Hu, H. R. Wang, Y. F. Zhu, J. Y. Li, Y. F. Liu, J. Q. Wang, H. X. Liu, X. B. Jia, H. W. Li, Y. Su, Y. Gao, S. Q. Chen, X. W. Wu, S. X. Dou, S. L. Chou and Y. Xiao, A Universal Strategy Based on Bridging Microstructure Engineering and Local Electronic Structure Manipulation for High-Performance Sodium Layered Oxide Cathodes, *ACS Nano*, 2023, **17**, 15871–15882.

9 Z. Y. Gu, J. Z. Guo, J. M. Cao, X. T. Wang, X. X. Zhao, X. Y. Zheng, W. H. Li, Z. H. Sun, H. J. Liang and X. L. Wu, An advanced high-entropy fluorophosphate cathode for sodium-ion batteries with increased working voltage and energy density, *Adv. Mater.*, 2022, **34**, e2110108.

10 J. Bareno, J. A. Gilbert, A. N. Jansen and S. Trask, Cycling behavior of NCM523/graphite lithium-ion cells in the 3–4.4 V range: diagnostic studies of full cells and harvested electrodes, *J. Electrochem. Soc.*, 2017, **164**, A6054.

11 Y. Su, B. Johannessen, S. L. Zhang, Z. R. Chen, Q. F. Gu, G. J. Li, H. Yan, J. Y. Li, H. Y. Hu, Y. F. Zhu, S. L. Xu, H. K. Liu, S. X. Dou and Y. Xiao, Soft-Rigid Heterostructures with Functional Cation Vacancies for Fast-Charging and High-Capacity Sodium Storage, *Adv. Mater.*, 2023, **35**, 2305149.

12 J. Bai, W. Sun, J. Zhao, D. Wang and F. Wang, Kinetic pathways templated by low-temperature intermediates during solid-state synthesis of layered oxides, *Chem. Mater.*, 2020, **32**, 9906–9913.

13 C. Hou, Y. Oaki, E. Hosono, H. Lin, H. Imai, Y. Fan and F. Dang, Bio-inspired synthesis of $xLi_2MnO_{3-(1-x)}LiNi_{0.33}Co_{0.33}Mn_{0.33}O_2$ lithium-rich layered cathode materials, *Mater. Des.*, 2016, **109**, 718–725.

14 Z. Hou, S. Xia, C. Niu, Y. Pang, H. Sun, Z. Li, Y. Xu and S. Zheng, Tailoring the interaction of covalent organic framework with the polyether matrix toward high-performance solid-state lithium metal batteries, *Carbon Energy*, 2022, **4**, 506–516.

15 H. R. Kim, S. G. Woo, J. H. Kim, W. Cho and Y. J. Kim, Capacity fading behavior of Ni-rich layered cathode materials in Li-ion full cells, *J. Electroanal. Chem.*, 2016, **782**, 168–173.

16 U.-H. Kim, N.-Y. Park, G.-T. Park, H. Kim, C. S. Yoon and Y.-K. Sun, High-energy W-doped $Li[N_{i0.95}Co_{0.04}Al_{0.01}]O_2$ cathodes for next-generation electric vehicles, *Energy Storage Mater.*, 2020, **33**, 399–407.

17 U. H. Kim, G. T. Park, B. K. Son, G. W. Nam, J. Liu, L. Y. Kuo, P. Kaghazchi, C. S. Yoon and Y. K. Sun, Heuristic solution for achieving long-term cycle stability for Ni-rich layered cathodes at full depth of discharge, *Nat. Energy*, 2020, **5**, 860–869.

18 Z. Y. Gu, J. Z. Guo, Z. H. Sun, X. X. Zhao, X. T. Wang, H. J. Liang, X. L. Wu and Y. C. Liu, Air/water/temperature-stable cathode for all-climate sodium-ion batteries, *Cell Rep. Phys. Sci.*, 2021, **2**, 100665.

19 M. Zubair, G. Li, B. Wang, L. Wang and H. Yu, Electrochemical kinetics and cycle stability improvement with Nb doping for lithium-rich layered oxides, *ACS Appl. Energy Mater.*, 2018, **2**, 503–512.

20 S. Y. Ryu, G. A. Wendt, C. E. Chandler, R. K. Ernst and D. R. Goodlett, Model-based spectral library approach for bacterial identification *via* membrane glycolipids, *Anal. Chem.*, 2019, **91**, 11482–11487.

21 H. Wang, K. Lai, F. Guo, B. Long, X. Zeng, Z. Fu, X. Wu, Y. Xiao, S. Dou and J. Dai, Theoretical calculation guided materials design and capture mechanism for Zn-Se batteries *via* heteroatom-doped carbon, *Carbon Neutralization*, 2022, **1**, 59–67.

22 G.-T. Park, N.-Y. Park, T.-C. Noh, B. Namkoong, H.-H. Ryu, J.-Y. Shin, T. Beierling, C. S. Yoon and Y.-K. Sun, High-performance Ni-rich $Li[Ni_{0.9-x}Co_{0.1}Al_x]O_2$ cathodes *via* multi-stage microstructural tailoring from hydroxide precursor to the lithiated oxide, *Energy Environ. Sci.*, 2021, **14**, 5084–5095.

23 Z. X. Huang, Z. Y. Gu, Y. L. Heng, E. H. Ang, H. B. Geng and X. L. Wu, Advanced layered oxide cathodes for sodium/potassium-ion batteries: Development, challenges and prospects, *Chem. Eng. J.*, 2023, **452**, 139438.

24 Y.-F. Zhu, Y. Xiao, S.-X. Dou, Y.-M. Kang and S.-L. Chou, Spinel/Post-spinel engineering on layered oxide cathodes for sodium-ion batteries, *eScience*, 2021, **1**, 13–27.

25 Y. Liu, L. B. Tang, H. X. Wei, X. H. Zhang, Z. J. He, Y. J. Li and J. C. Zheng, Enhancement on structural stability of Ni-rich cathode materials by in-situ fabricating dual-modified layer for lithium-ion batteries, *Nano Energy*, 2019, **65**, 104043.

26 J. H. Kim, S. J. Kim, T. Yuk, J. Kim, C. S. Yoon and Y. K. Sun, Variation of electronic conductivity within secondary particles revealing a capacity-fading mechanism of layered Ni-rich cathode, *ACS Energy Lett.*, 2018, **3**, 3002–3007.

27 P. Li, Y. Bu, L. Wang, C. Wang, J. Huang, K. Tong, Y. Chen, J. He, Z. Zhao, B. Xu, Z. Liu, G. Gao, A. Nie, H. Wang and Y. Tian, In situ observation of fracture along twin boundaries in boron carbide, *Adv. Mater.*, 2022, e2204375, DOI: **10.1002/adma.202204375**.

28 Z. Y. Gu, Y. L. Heng, J. Z. Guo, J. M. Cao, X. T. Wang, X. X. Zhao, Z. H. Sun, S. H. Zheng, H. J. Liang, B. Li and X. L. Wu, Nano self-assembly of fluorophosphate cathode induced by surface energy evolution towards high-rate and stable sodium-ion batteries, *Nano Res.*, 2022, **16**, 439–448.

29 I. Hamam, R. Omessi, D. Rathore, C. Geng, R. Cooke, K. Plucknett, D. P. Bishop, N. Zaker, G. A. Botton and C. Yang, Correlating the mechanical strength of positive electrode material particles to their capacity retention, *Cell Rep. Phys. Sci.*, 2022, **3**, 100714.

30 C. Geng, S. Trussler, M. B. Johnson, N. Zaker and J. R. Dahn, A low-cost instrument for dry particle fusion coating of advanced electrode material particles at the laboratory scale, *J. Electrochem. Soc.*, 2020, **167**, 110509.

31 J. Li, H. Hu, J. Wang and Y. Xiao, Surface chemistry engineering of layered oxide cathodes for sodium-ion batteries, *Carbon Neutralization*, 2022, **1**, 96–116.

32 H.-H. Ryu, G.-T. Park, C. S. Yoon and Y.-K. Sun, Suppressing detrimental phase transitions *via* tungsten doping of $LiNiO_2$ cathode for next-generation lithium-ion batteries, *J. Mater. Chem. A*, 2019, **7**, 18580–18588.

33 U. H. Kim, D. W. Jun, K. J. Park, Q. Zhang, P. Kaghazchi, D. Aurbach, D. T. Major, G. Goobes, M. Dixit, N. Leifer, C. M. Wang, P. Yan, D. Ahn, K. H. Kim, C. S. Yoon and Y. K. Sun, Pushing the limit of layered transition metal oxide cathodes for high-energy density rechargeable Li ion batteries, *Energy Environ. Sci.*, 2018, **11**, 1271–1279.

34 K. Yuan, N. Li, R. Ning, C. Shen, N. Hu, M. Bai, K. Zhang, Z. Tian, L. Shao, Z. Hu, X. Xu, T. Yu and K. Xie, Stabilizing surface chemical and structural Ni-rich cathode *via* a non-destructive surface reinforcement strategy, *Nano Energy*, 2020, **78**, 105239.

35 C. Geng, D. Rathore, D. Heino, N. Zhang, I. Hamam, N. Zaker, G. A. Botton, R. Omessi, N. Phattharasupakun, T. Bond, C. Yang and J. R. Dahn, Mechanism of action of the tungsten dopant in $LiNiO_2$ positive electrode materials, *Adv. Energy Mater.*, 2021, **12**, 2103067.

36 L. Ni, R. Guo, S. Fang, J. Chen, J. Gao, Y. Mei, S. Zhang, W. Deng, G. Zou, H. Hou and X. Ji, Crack-free single-crystalline Co-free Ni-rich $LiNi_{0.95}Mn_{0.05}O_2$ layered cathode, *eScience*, 2022, **2**, 116–124.

37 Z. Kong, M. L. Huang, K. Zhang, Z. Y. Liang, H. Y. Tu, Y. L. Shao, Y. Z. Wu and X. P. Hao, Twin boundary $Cd_xZn_{1-x}S$: a new anode for high reversibility and stability lithium/sodium-ion batteries, *J. Mater. Chem. A*, 2022, **10**, 23799–23810.

38 R. Wang, X. Chen, Z. Huang, J. Yang, F. Liu, M. Chu, T. Liu, C. Wang, W. Zhu, S. Li, S. Li, J. Zheng, J. Chen, L. He, L. Jin, F. Pan and Y. Xiao, Twin boundary defect engineering improves lithium-ion diffusion for fast-charging spinel cathode materials, *Nat. Commun.*, 2021, **12**, 3085.

39 H. Y. S. Chung, Y. X. Li, M. H. Zhang, A. Grenier, C. Mejia, D. Y. Cheng, B. Sayahpour, C. Y. Song, M. H. Shen, R. C. Y. Huang, E. A. Wu, K. W. Chapman, S. J. Kim and Y. S. Meng, Mitigating anisotropic changes in classical layered oxide materials by controlled twin boundary defects for long cycle life Li-ion batteries, *Chem. Mater.*, 2022, **34**, 7302–7312.

40 Z. Z. Li, X. Huang, J. N. Liang, J. L. Qin, R. Wang, J. G. Cheng and D. L. Wang, Element doping induced microstructural engineering enhancing the lithium storage performance of high-nickel layered cathodes, *J. Energy Chem.*, 2023, **77**, 461–468.

41 B. Namkoong, N. Y. Park, G. T. Park, J. Y. Shin, T. Beierling, C. S. Yoon and Y. K. Sun, High-energy Ni-rich cathode materials for long-range and long-life electric vehicles, *Adv. Energy Mater.*, 2022, **12**, 2200615.